*fire*

MDPI

*Article*

# Numerical Study of the Effect of the Ignition Procedure on the Front of a Surface Fire from a 3D Numerical Model

**Akahoua D. V. Brou**

Laboratoire des Sciences et Technologies de l'Environnement, Département Mathématiques-Phsique-Chimie-Informatique, UFR Environnement, Université Jean Lorougnon Guédé de Daloa, Daloa BP 150, Côte d'Ivoire; brou.akahoua@ujlg.edu.ci

**Abstract:** In instrumented prescribed fires, the ignition procedure requires much attention. In this paper, we investigate the effects of two ignition procedures on the fire head using a 3D numerical model. The first procedure is to ignite the fire from the edges of the fire line towards the centre of the line. The second procedure consists of igniting the fire from the centre of the fire line to the edges of the line. The 3D numerical model used is based on the modelling of the fuel layer from Lagrangian particles, and the fire propagation is based on a two-phase model. The model was tested on an experimental fire in a wheat field in southern Australia. The model predicted the experimental fire front well. Analysis of the impact of the ignition procedure on the fire head showed that the quasi-steady-state rate of fire spread was the same for both procedures. However, before the quasi-stationary state, the front of the first procedure spread faster than that of the second procedure. The fire front in the first procedure was wider than in the second procedure. It was also found that the length of the head fire in the first procedure remained the same as that of the ignition line. In the second procedure, the length of the head fire was one-third of that of the ignition line.

**Keywords:** 3D numerical model; Lagrangian particles; ignition procedure; rate of spread; vegetation fire front



**Citation:** Brou, A.D.V. Numerical Study of the Effect of the Ignition Procedure on the Front of a Surface Fire from a 3D Numerical Model. *Fire* **2023**, *6*, 15. https://doi.org/10.3390/fire6010015

Academic Editor: Ali Cemal Benim

Received: 14 December 2022
Revised: 30 December 2022
Accepted: 1 January 2023
Published: 4 January 2023



## 1. Introduction

In wildland fire experiments, the ignition procedure is one of the important issues to be addressed. The objective is for the fire front to develop relatively quickly and have a quasi-stable progression [1]. In this paper, we analyse the effect of the ignition procedure on the fire front. Indeed, the ignition procedure can have an effect on the fire front and also on the rate of fire spread [1–4].

In the experiments by Cheney et al. (1993, 1995, 1998), two teams set fire to a minimum 25 m line on the upwind edge of the plot. The fire was ignited from the centre of the fire line towards the edges of the line [2,5,6]. According to Mell et al. (2007), the initial rapid spread of the fire depends on the ignition procedure and is worth investigating [3]. The ignition procedure used by Cruz et al. (2020) in their experiments consisted of igniting a 33 m fire line on the upwind edge of the plot. The fire was ignited by two teams from the edges of the fire line towards the centre of the line [1,4]. This procedure, according to Cruz et al. (2020), resulted in a continuous fire front quite quickly, which ensured a quasi-stationary spread of the fire front.

Numerical modelling and simulation can guide field-scale experiments and help to make decisions in a rational way to achieve experimental objectives.

In this paper, we investigate the effect on the fire front of two ignition procedures used by Australian researchers with proven expertise in instrumented prescribed fires. The first procedure is to ignite the fire from the edges of the fire line towards the centre of the fire line (edge-to-centre). The second procedure is to ignite the fire from the centre of the fire line to the edges of the fire line (centre-to-edge).

The effect of the two ignition protocols (presented above) on grass fire development was studied by Sutherland et al. (2019) using a physics-based simulation. The spread rate was the main variable analysed. The objective was to determine the procedure that achieved a quasi-stationary fire spread in a relatively short time as a function of wind speed, ignition time, and ignition line length [7]. We did not analyse the effect on the fire front, including the characteristics of the fire front, the interactions of the fire front with the unburned fuel ahead, and the interactions with the ambient air.

It is increasingly recognised that the structure of the fuel layer influences wildland fire behaviour [8]. Certain fire behaviours can only be obtained by modelling if the spatial structure of the fuel layer is taken into account in the models. According to Vanella et al. (2021), the fire front can have a complex shape that spreads and deforms according to local conditions, such as fuel load [9].

To study the effect of the ignition procedure on the fire front, we modelled the spatial distribution of the fuel layer using Lagrangian particles. This modelling is based on the fuel load and its height. It allows us to have a fuel layer structure that is closer to reality and that takes into account the heterogeneity of certain structural variables of the fuel layer. We simulate the fire spread within the fuel layer with a 3D two-phase model. The prediction of the fire front using our model is evaluated based on well-documented experiments performed in Australia by Cruz et al. (2020) [1]. After this test, we analyse the effect of the two ignition procedures indicated above on the fire front. The ignition line length and wind speed remain constant during the simulations.

## 2. Physical and Mathematical Model

The mathematical model is based on a two-phase formulation. It is three-dimensional and considers the coupled physicochemical processes that take place in both phases: the thermal degradation of organic matter, as well as turbulence, flaming combustion, soot formation, and radiation for the gas phase. These equations are given in the Appendix A. The mathematical details of the model have been presented in previous publications [10–12].

In this section, we present a modelling of the grass fuel bed. This one consists of several tussocks of grass, and we assume that all the blades of grass of a given tussock cross at the same point $O$, as shown in Figure 1. Further, we assume that each blade of grass has a cylindrical shape so that a point $M$ on the blade of grass is given by its coordinates

$$\vec{OM} = R\sin\theta\cos\phi\,\vec{e}_x + R\sin\theta\sin\phi\,\vec{e}_y + R\cos\theta\,\vec{e}_z \quad (1)$$

where $\theta \in [0;\pi/2]$ and $\phi \in [0;2\pi]$ are the directional angles of the blade of grass. The distance $R = OM$ is less than or equal to the length of the grass blade.

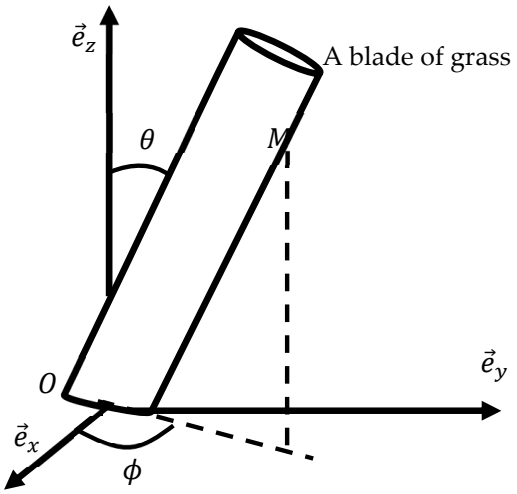


**Figure 1.** Presentation of the coordinate system and point $M$ on a blade of grass.

The fuel load is the indicator of the quality of the modelled herbaceous layer. The total number of grass blades $N_p$ is related to the fuel load by the relation

$$N_p = \frac{S_T W_s}{\rho_s V_p}. \tag{2}$$

where $W_s$ is the fuel load and $\rho_s$ and $h_s$ are its density and height, respectively. The total soil area occupied by the fuel layer is $S_T$ while $V_p$ is the volume of a blade of grass. This volume is calculated by the relation

$$V_p = \pi \frac{D_p^2}{4} h_s \tag{3}$$

where $D_p$ is the diameter of the grass blade particle. Some types of grass have diameters of $\mathcal{O}(0.1)$ mm. With such diameters, the calculation time is very expensive.

To avoid this difficulty, we assume that a cylindrical fuel particle is a collection of small-diameter cylindrical particles. In this study, the diameters used are $\mathcal{O}(1)$ mm. However, these diameters must be strictly less than 6mm. According to Morvan (2007), in a vegetation fire, it is the fine elements with a diameter of less than 6 mm that burn. For our simulations, we used 2 mm as the diameter of the cylindrical particle.

The computation domain is divided into several cells. The fuel layer model is inserted into the gas phase mesh. Each cell in the mesh may contain part of a blade of grass, parts of more than one blade of grass, or an area where there is no blade of grass. The packing ratio $\alpha_s$, which is the fraction of the fuel bed volume occupied by the fuel particle, is

$$\alpha_s = \frac{n_p V_p}{V_c} \tag{4}$$

where $n_p$ is the number of solid particles in a cell and $V_c$ is the volume of a cell. The volume of the solid particle $V_p$ is calculated using relation (3), taking the height of the particle $h_p$ instead of $h_s$. The packing ratio is, therefore, not uniform and can vary from one cell to another. The fuel bed is horizontally and vertically non-uniform. The specific area $A_s$ of the solid phase in a cell is determined by

$$A_s = \frac{n_p S_p}{V_c} \tag{5}$$

where $S_p$ is the surface area of the particle and depends on the diameter of the grass blade. The surface-to-volume ratio $\sigma_s$ is also computed using the following relation

$$\sigma_s = \frac{A_s}{\alpha_s} \tag{6}$$

In the following, we present the solid-phase decomposition model approach and its ignition. The fuel receives heat from the fire front by radiation as well as by convection of hot gases. This heat raises the temperature $T_s$ of the grasses to the evaporation temperature of water ($T_s = 373$K). As indicated by several authors [13–18], the dehydration process starts slowly at low temperatures and ends around 373 K. The same is true for pyrolysis, which takes place between 400 K and 500 K. The model explained above gives in terms of equations

$$\begin{cases} \alpha_s \rho_s C_{ps} \frac{\partial T_s}{\partial t} = Q_{rad} + Q_{conv} & \text{if } T_s \neq 373\ K \text{ or } T_S \neq 500\ K (a) \\ \dot{m}_{H_2O} = \frac{Q_{rad}+Q_{conv}}{L^{H_2O}} & \text{if } m_{H_2O} > 0 \text{ and } T_s = 373\ K (b) \\ \dot{m}_{pyr} = \frac{Q_{rad}+Q_{conv}}{L^{pyr}} & \text{if } m_{pyr} > 0 \text{ and } 400\ K \leq T_s \leq 500\ K (\text{c}) \end{cases} \tag{7}$$

where $\alpha_s$ is the volume fraction of the solid, $\rho_s$ is the fuel density, and $C_{ps}$ its specific heat. Radiative heat transfer can occur in two ways: surface radiation ($Q_{radsurf}$) and

internal radiation ($Q_{radint}$). The heat flux received by radiation is $Q_{rad} = Q_{radint} + Q_{radsurf}$; $Q_{conv}$ represents the convective exchange with the surrounding gas. The mass of the water contained in the grasses is $m_{H_2O}$. The heat of water evaporation $L^{H_2O}$ is equal to $2.25 \times 10^6$J/kg. The rate at which water vapour is generated is $\dot{m}_{H_2O}$. Similarly, pyrolysis occurs when the fuel temperature is at 400 K. Several authors have used a similar approach to model the degradation of solid fuel [3,19,20]. The rate at which fuel gas is generated is $\dot{m}_{pyr}$. The heat of pyrolysis $L^{pyr}$ is equal to $0.418 \times 10^6$J/kg, and $m_{pyr}$ is the mass of gaseous fuel contained in the grasses.

The convective heat $Q_{conv}$, received by the grass is as follows

$$Q_{conv} = A_s h_s (T - T_s) \tag{8}$$

where $T$ and $T_s$ are the temperature of the gas and the solid, respectively, while $h_s$ is the convection–conduction heat transfer coefficient. For a cylinder, this coefficient is given by [21] as $h_s = 0.683\lambda Re_s^{0.466}/2r_s$. The thermal conductivity is $\lambda$, and the Reynolds number $Re_s$ is based on the radius $r_s$ of the cylindrical particle.

The unburned fuel receives radiative heat flux through the fuel bed volume from the flame front ($Q_{radsurf}$). The surface radiation is defined as follows

$$Q_{radsurf} = \alpha_s \frac{A_s}{4}\left(G - 4\sigma T_s^4\right) \tag{9}$$

where the average incident radiation $G = \int_{4\pi} I\left(\vec{\Omega}\right) d\Omega$. The radiation intensity $I\left(\vec{\Omega}\right)$ in the $\vec{\Omega}$ direction is calculated by solving the radiation transfer equation (RTE). As mentioned by De Mestre et al. (1989), the absorption coefficient can be calculated from the standard formula: $\frac{A_s}{4}$ [22].

Burning fuel embers lose heat from radiative transfer ($Q_{radint}$), and this heat contributes to the preheating of unburned fuel elements [19,23]:

$$Q_{radint} = \sum_{i=1}^{N_{fire}} 0.25 A_s \varepsilon_{fl} \sigma T_{ifl}^4 \exp(-0.25 A_s d_i) \tag{10}$$

where $N_{fire}$ is the number of cells in the front line of the fire, $T_{ifl}$ is the temperature of the burning cell I, and $d_i$ the distance between the cell i and the unburned fuel. The Stephan–Boltzmann constant is $\sigma (= 5.67 \times 10^{-8}\mathrm{W/m^2/K})$. The flame emissivity $\varepsilon_{fl}$ is expressed as [24]

$$\varepsilon_{fl} = 1 - \exp(-0.6\Delta z) \tag{11}$$

where $\Delta z$ is the height of the cell within the fuel bed.

In grassland fires, after the fire front passes, the structure of the fuel bed collapses. This allows the wind to blow the base of the flame and push the fire front forward. The dehydration of the solid and its pyrolysis leads to a decrease in its volume. Therefore, the volume fraction of the solid and the volume fraction of the gas are updated each time. The gas volume fraction $\alpha_g$ is given by the equation $\alpha_g = 1 - \alpha_s$. The volume fraction of the solid $\alpha_s$ is calculated using the equations given above. This change in volume also leads to a change in specific area $A_s$ of the solid phase.

Most of the grass is converted to gaseous fuel since grass has a low char content (about 20% [25]). Therefore, the effect of char oxidation on fire spread is neglected.

The vertical wind speed profile is calculated using the Dupuy and Morvan (2005) model [26], namely

$$U(z) = U_H \left(\frac{z}{H}\right)^{1/7} \tag{12}$$

where $U_H$ is the wind speed at height $H$.

## 3. Results

The fuel layer model presented in the previous section is used to simulate the fire spread. Figure 2 shows the modelling of a grass layer with a load of 0.6 kg·m$^{-2}$ and a height of 0.29 m.

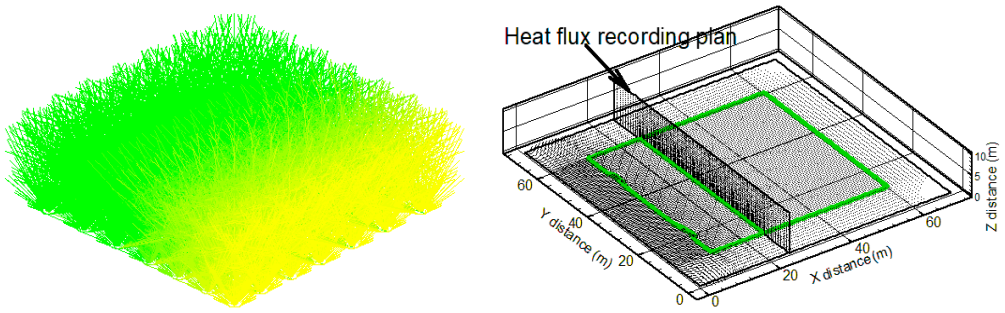


(**A**) (**B**)

**Figure 2.** Presentation of the numerical fuel bed model and the computational domain: (**A**) Modelling of a grass layer with a load of 0.6 kg·m$^{-2}$ and a height of 0.29 m; (**B**) Computational domain and plan for heat flux recording. The wind speed field is in black, and the limits of the fuel layer are in green.

Before simulating field-scale fire experiments, several tests of the independence of the model solution with respect to cell size were performed. According to Moinuddin et al. (2018) [27], if the predicted spread rate is close to that of the smallest grid size, then the model results are independent of the grid size. This property has been verified for cell sizes equal to 1 m in the horizontal direction and of variable sizes in the vertical direction. Details of this study can be found in [12]. Therefore, the cell sizes indicated above will be used for the next simulations. The time step is set to 0.05 s.

A distance of 10 m is maintained between the fuel layer and the boundaries. This is to avoid the impact of a nonphysical numerical flow due to the proximity of the boundaries (see Figure 2B).

### *3.1. Overview of Surface Fire Experiments*

Cruz et al. (2020) [1] conducted several experimental fires in wheat crops in southern Australia. The objective of these experiments conducted on 50 m × 50 m sites was to study the behaviour of fire in a wheat field and to assess the adequacy of existing operational prediction models used for these fuel types. The comparisons showed that the fire spread rate corresponded directly to the outputs of the Cheney et al. (1998) grass fire models. We, therefore, used one of those experiments to test our model. Indeed, the fuel layer in our model is of the grass layer type. The simulated fire experiment was the WH21 experiment. This was the only experiment for which we had aerial images of the fire perimeter at 21 s, 29 s, and 37 s. The input data used for the simulation are presented in Table 1. The ignition line is 33 m long and was carried out by two teams for 10 s. The fire was ignited from the edges of the fire line towards the centre of the fire line on the upwind side of the site. This ignition protocol was followed during the simulations. Figure 3A shows the simulated fire start.

**Table 1.** Weather characteristics, fuel structure, and fuel moisture content (Cruz et al., 2020).

| Property | Units | WH21 Experiment |
|---|---|---|
| Air temperature | K | 305.5 |
| 2-m wind speed | m/s | 6.19 |
| Fuel moisture content | % | 6.1 |
| Fuel load | Kg/m$^2$ | 0.394 |
| Fuel bed height | m | 0.29 |

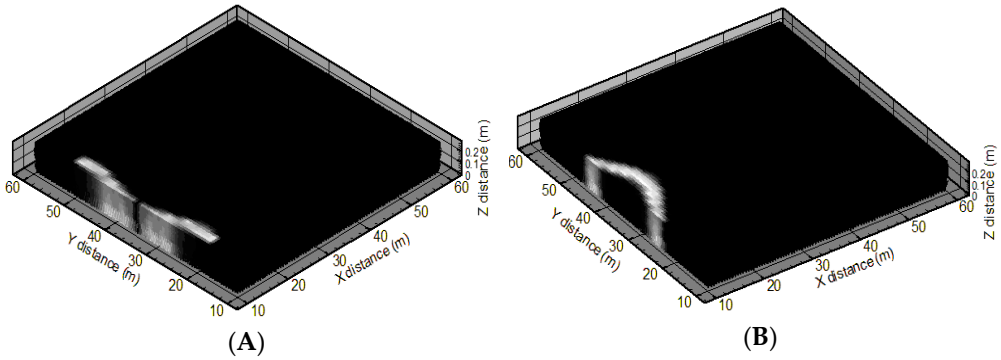


**Figure 3.** Ignition line after 7 s: (**A**) edge-to-centre ignition and (**B**) centre-to-edge ignition. The edge of the light is marked by any temperature above 500 K.

Cruz et al. placed reference markers at 10 m intervals to follow the fire front across the plot. The first row of reference markers was located approximately 19 m from the ignition line. The fire front, 21 s after the fire started, reached this first row. At 29 s, the fire front was between the second and third row of reference markers, i.e., between 29 m and 39 m from the ignition line. At 37 s, the fire front was at the edge of the experimental plot.

### *3.2. Validation Case*

In this paper, the ability of our model to predict fire behaviour was tested from the fire front. No reference marker was positioned to follow the evolution of the flanking fire (fire spreading in the direction more or less perpendicular to the wind). Therefore, the comparison will focus on the head of the fire (fire spreading in the wind direction).

Figure 4 presents a top view of the fire front during the WH21 experiment (Figure 4 column A) and the one predicted by our model (Figure 4 column B) at 21 s, 29 s, and 37 s after the fire started. It should be noted that the ignition line in our simulations was located 10 m from the boundary of the computational domain.

As can be seen, the predicted fire front at 21 s is about 20 m from the ignition line. This is in agreement with the observed position of the fire front at the same time. The predicted fire front at 29 s was between 30 m and 40 m from the ignition line. The observed one was between 29 m and 39 m. These two fronts are, therefore, in good agreement. At 37 s, the observed fire front reached the limit of the experimental site. This was not the case for the predicted fire front, which was 5 m from the edge of the vegetated area. The model, therefore, underestimated the position of the fire front. The flank of the fire observed at 37 s was closer to the lateral firebreak of the plot than predicted. The propagation mechanism in a flank fire is complex and is the subject of research within the scientific community [3]. However, according to Vanella et al. (2021), models based on Lagrangian particles improve the flank fire spread rates. This is the case here: although there was an underestimation, it was relatively small. The lack of reference markers for the fire flank did not allow a quantitative comparison. However, it can be observed overall that the perimeter was relatively well predicted by our model.

### *3.3. Effect of the Ignition Procedure on the Fire Front*

In this section, the previously tested model is used to study the effect of the ignition procedure on the fire front. In the design of the experimental protocol, the ignition procedure is one of the important issues to be addressed. In this paper, we study two ignition procedures. In the first procedure, the fire is ignited from the edges towards the centre of the ignition line (edge-to-centre ignition). In the second procedure, the fire is ignited from the centre of the ignition line towards the edges (centre-to-edge ignition). The ignition is carried out by two teams in both procedures. The length of the ignition line is 33 m, and the ignition time is 10 s, as in the experiment simulated in the previous section. This experiment was well-predicted and will be used as the basis for our study. Therefore, the

fuel characteristics and the dimensions of the computational domain are the same as in the validation test.

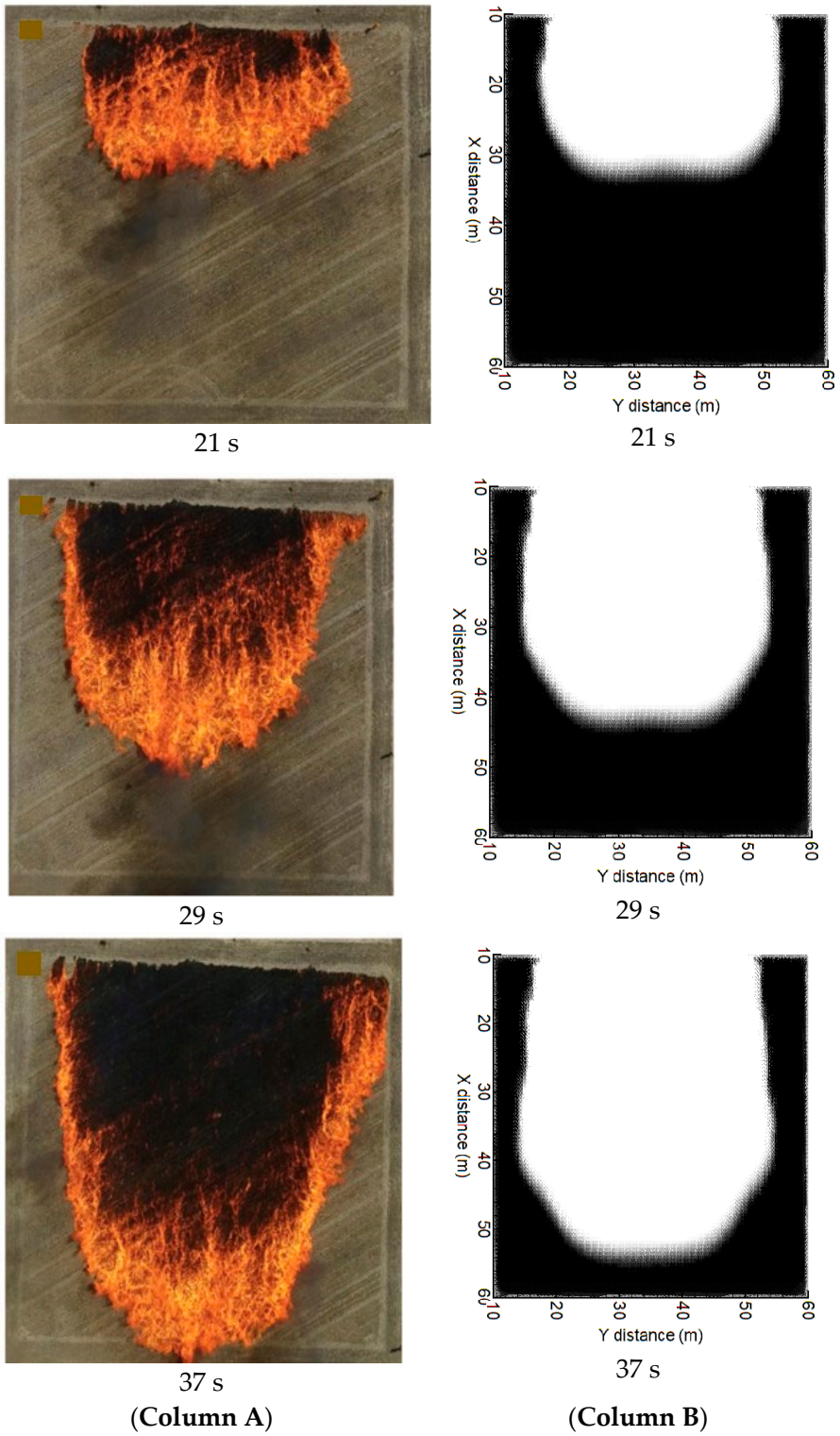


**Figure 4.** Image and simulation of the fire contour of the WH21 experimental: (**Column A**) aerial view of the WH21 experimental fire; (**Column B**) top view of the predicted fire contour plotted from the fuel volume fraction. White is the vegetation consumed by the fire, and black is the healthy vegetation.

Figure 5 shows the fire front at times 21 s, 29 s, and 37 s with the edge-to-centre ignition (Figure 5 column A) and the centre-to-edge ignition (Figure 5 column B). The fire front is

located at any temperature above 500 K. It can be seen from this figure that the fire front for the edge-to-centre ignition is wider than that for the centre-to-edge ignition. The length of the fire head for the edge-to-centre ignition is about 30 m. This length is close to that of the ignition line. The length of the fire head for the centre-to-edge ignition is about 10 m, which is about one-third of the length of the ignition line. This shape is observed at all three times.

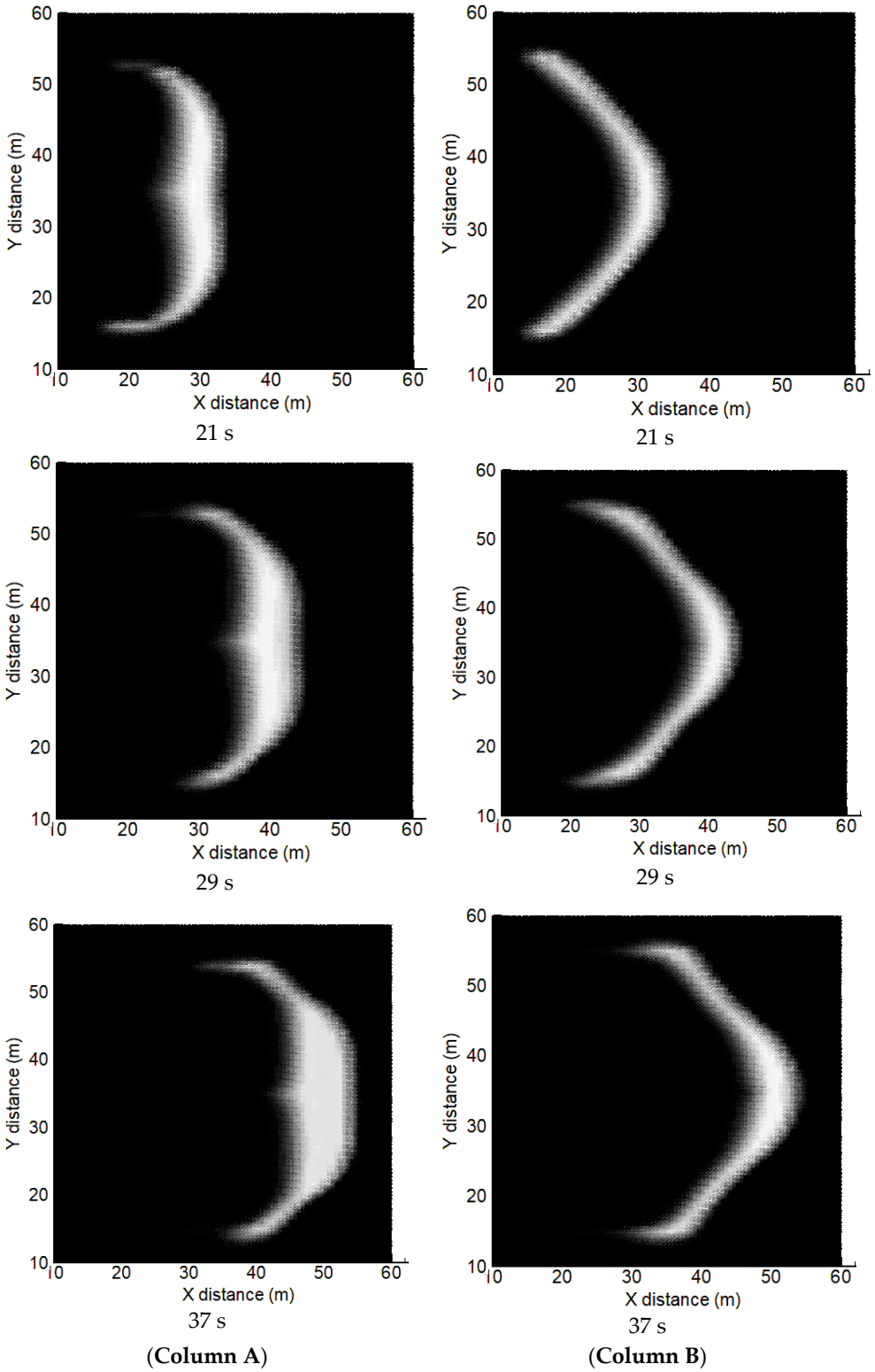


**Figure 5.** Fire contour at different times marked by temperatures above 500 K: (**Column A**) edge-to-centre ignition; (**Column B**) centre-to-edge ignition.

Figure 6 compares the positions of the pyrolysis front as a function of time for both procedures, as well as the heat release rate (HRR). The HRR is calculated by the formula

$$HRR = \sum_{FR} \dot{m}_{pyr}.V_c.\Delta h_c, \quad (13)$$

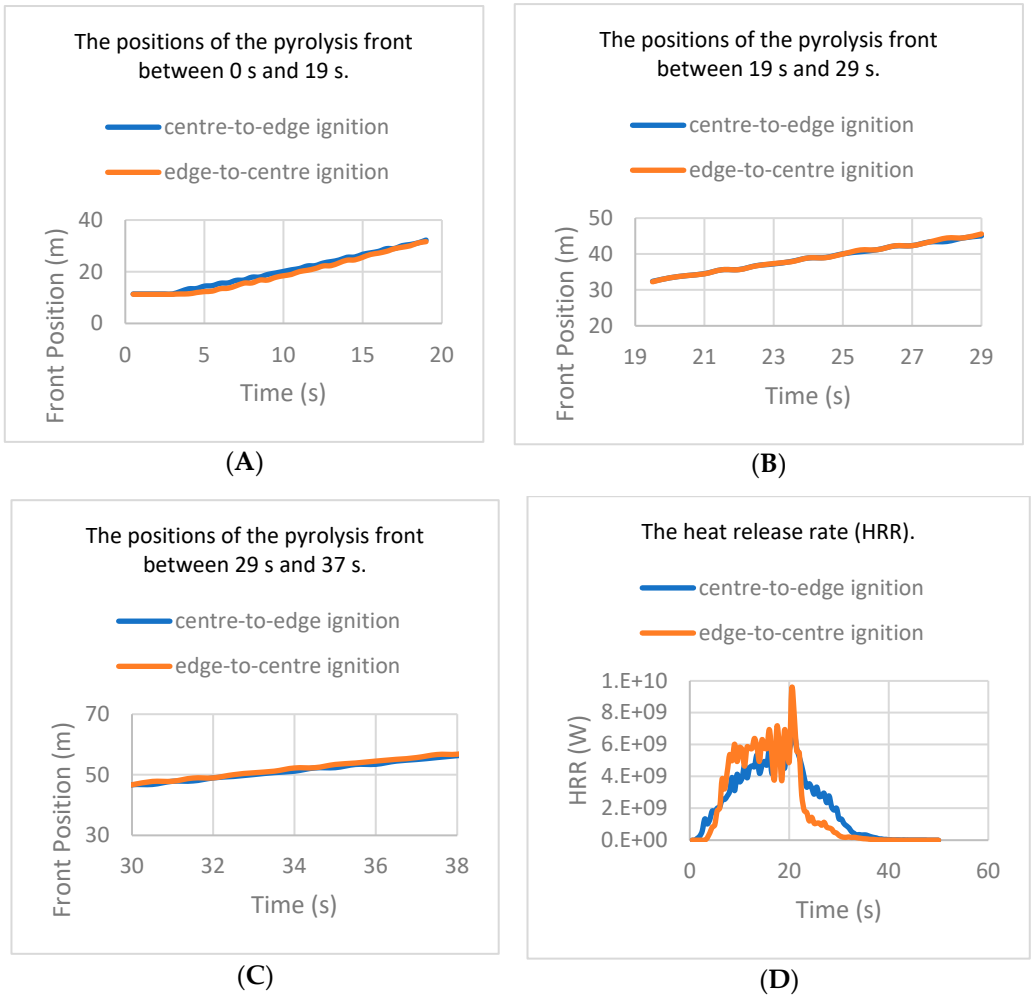


**Figure 6.** Comparison of predicted fire front positions and heat release rates for the two ignition procedures. (**A**) The positions of the pyrolysis front between 0 s and 19 s. (**B**) The positions of the pyrolysis front between 19 s and 29 s. (**C**) The positions of the pyrolysis front between 29 s and 37 s. (**D**) The heat release rate (HRR).

*FR* is the fire region and $\Delta h_c$ is the heat of combustion.

The positions of the pyrolysis front under 19 s after the start of the fire are shown in Figure 6A. The positions of the pyrolysis front between 19 s and 29 s are shown in Figure 6B, and those between 29 s and 37 s are shown in Figure 6C. These different time intervals were chosen according to the aerial images of the fire perimeter for the WH21 experiment. Indeed, these times coincide with those of the aerial images. It can be seen that before 19 s, the curve of the centre-to-edge ignition was above that of the edge-to-centre ignition. The fire front of the centre-to-edge ignition, therefore, spreads faster than that of the edge-to-centre ignition (Figure 6A). Between 19 s and 29 s on the one hand and 29 s and 37 s on the other, the spread of the fire front is the same for both procedures (Figure 6B,C). Looking at Figure 6D, it can be seen that the edge-to-centre ignition generates much more heat than the other ignition procedure.

Figure 7 shows the fire front at the mid-height of the fuel layer as well as the streamlines for both ignition procedures 20 s after the fire was started. Figure 8 shows the evolution of

the heat fluxes as a function of distance in the x = 25 m plane at the same time (This plane is shown in Figure 2B). This plane is perpendicular to the direction of the fire spread and is located just in front of the fire front. This allows us to analyse the effect of the ignition procedure on the heat transfer. By observing the streamlines, we can see a significant recirculation at the edges of the fire line for both procedures. This recirculation causes fresh air to be drawn in. Figure 8C, which shows the convective heat flow, reveals that the cooling at the edge of the fire line is greater than that in the centre for the edge-to-centre ignition. For the centre-to-edge ignition, the cooling is observed near the centre of the fire line.

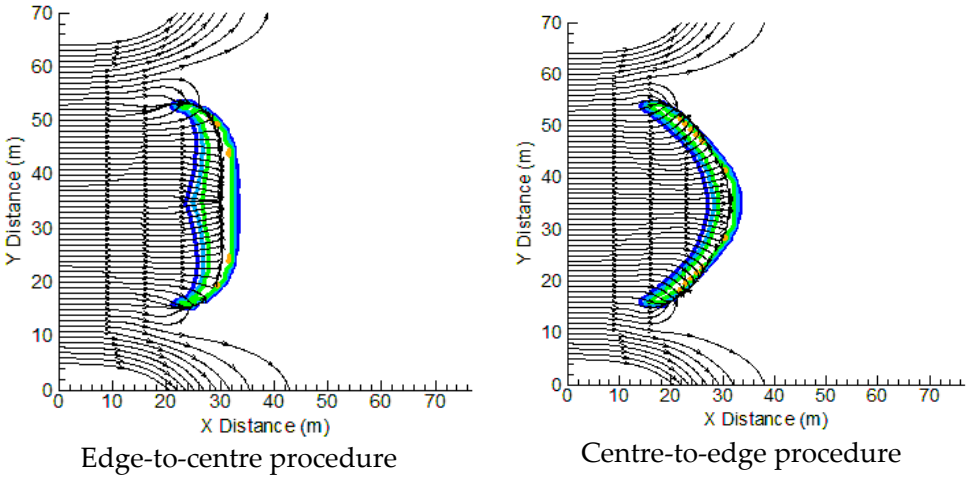


**Figure 7.** Fire contours and streamlines at mid-height of the fuel layer 20 s after the fire started. The fire contour is located at temperatures above 500 K.

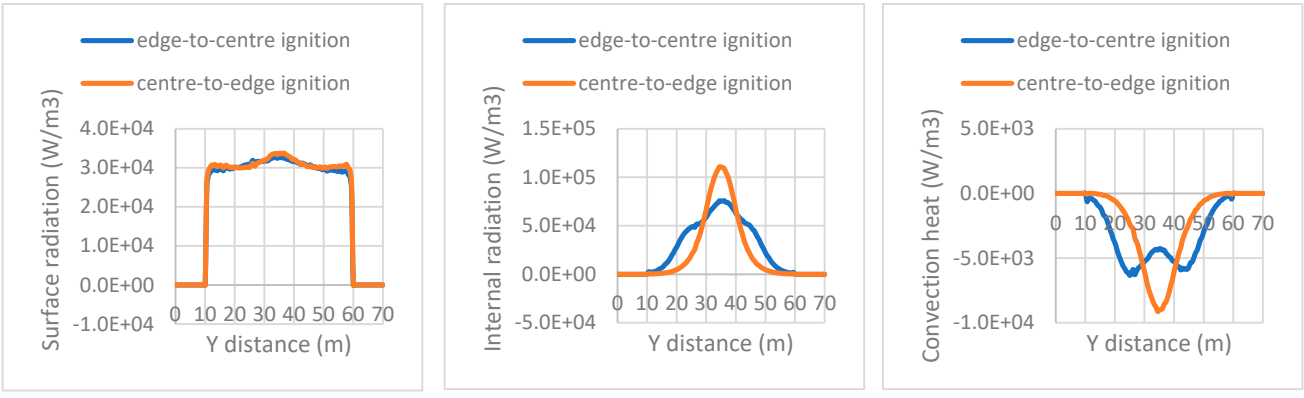


**Figure 8.** Heat fluxes as a function of distance in the plane x = 25 m, perpendicular to the direction of fire spread, 20 s after the start of the fire: (**A**) Heat flux due to flame radiation; (**B**) Heat flux due to ember radiation; (**C**) Heat flux due to convection.

While the radiation from the flame is the same for both procedures (Figure 8A), the radiation from the embers is different. Indeed, the radiation from the embers at the centre of the fire line is higher for the centre-to-edge ignition than for the edge-to-centre ignition (Figure 8B). It can also be observed that the radiation from the embers is mainly between 20 m and 50 m for the edge-to-centre ignition. However, for the centre-to-edge ignition, the radiation from the embers is significant between 30 m and 40 m. The same is true for the convective flow (Figure 8C).

### *3.4. Discussion*

The ignition procedure has an effect on the dimensions of the fire front (length and width), on the convective flux, and on the radiation of the embers. The radiation of the flame front is identical for both procedures. The fire spread rates are different in the first few seconds after the start of the fire. Indeed, below 19 s, the fire front of the centre-to-edge ignition spreads slightly faster than that of the other procedure (Figure 6A). After 19 s, both fronts reach a quasi-stationary spread and move almost at the same speed (Figure 6B,C). The initial rapid progression of the front was highlighted by Mell et al. (2007), who suspected the ignition procedure [3]. Simulation results in our context show that the ignition procedure has no real effect on the spread rate, especially in the quasi-stationary propagation regime. Moreover, the quasi-stationary propagation is reached almost at the same time for both procedures.

The recirculation of gases at the edges of the fire line is the basis of the shape of the fire line. Indeed:

- For edge-to-centre ignition

Figure 8C shows significant cooling at the edges of the fire line. This proves that the gas recirculation at the edges is more important than at the centre of the fire line. This is because gas recirculation causes fresh air to be drawn towards the fire front. The combined effect of recirculation, which disrupts the flow of gases in the wind direction (Figure 7), and the cooling of the fuel upwind of the fire front allows the fire in the centre to rise to the level of the fires at the edges of the fire line. This explains why the length of the fire head is close to the length of the ignition line (Figure 5, column A).

- For centre-to-edge ignition

The observed recirculation (Figure 7) disrupts the gas flow at the edges of the fire line. This allows the fire in the centre of the line to overtake the fires at the edges of the fire line. The latter become flanking fires (fire propagating in the direction more or less perpendicular to the wind direction). This is illustrated in Figure 8B,C, which show that the heat transfer to the fuels ahead of the fire front is due to the head of the fire between 30 m and 40 m. The strong cooling in the centre (Figure 8C) is attenuated by the strong radiation in the centre as well (Figure 8A,B).

Ember radiation and convection are related to the shape of the fire front, as shown in Figures 5 and 8B,C. Indeed, in Figure 5, we can see that the fire front is located between 20 m and 50 m for the edge-to-centre ignition and between 30 m and 40 m for the centre-to-edge ignition. Moreover, in Figure 8B,C, the intervals in which internal radiation and convection are significant are the same as those shown above.

The fire head in the edge-to-centre ignition is wider than in the centre-to-edge ignition (see Figures 5 and 7). This result is consistent with experimental observations [1,2,5]. It could be explained by the greater intake of fresh air for the edge-to-centre ignition, which results in the widening of the combustion zone. This width could explain the high heat release rate of this procedure.

Another important result is that the fire head in the edge-to-centre ignition keeps the same length as the ignition line. However, the length of the fire head in the centre-to-edge ignition is one-third of that of the ignition line.

The results obtained here were obtained within a specific framework: the length of the ignition line and the wind speed did not vary for the two procedures. The length of the ignition line was 33 m, and the dimensions of the site were 50 m $\times$ 50 m. The simulation allowed us to understand some of the effects of the ignition procedure on the size of the fire front, the interaction of the fire front with the surrounding air, and the heat transferred to the fuel ahead of the front.

The number of simulations presented here is not sufficient to provide conclusive results on all the interdependencies that occur in the simulations, but it is sufficient to inspire many new questions and to guide future research directions.

## 4. Conclusions

We studied the effect of two ignition procedures on the fire front using a 3D numerical fire spread model. This model is based, on the one hand, on the modelling of the fuel layer from Lagrangian particles and, on the other hand, on a two-phase spread model.

This model was tested on an experimental fire in a wheat field in southern Australia. Agreement was found between the predicted and observed fire fronts.

Investigation of the effect of the two ignition procedures revealed that there was no significant difference in the quasi-stationary spread rate of the fire front. The steady state was reached almost at the same time for both procedures. The length of the fire head in the edge-to-centre ignition remained the same as that of the ignition line. However, for the centre-to-edge ignition, the length of the fire head was one-third of that of the ignition line. The study also revealed that the width of the fire head in the edge-to-centre ignition was wider than in the other procedure and gave off more heat. Gas recirculation had an important impact on the shape of the fire front and its dimensions.

Firefighting methods should be adapted to the ignition procedure. Furthermore, the length of the fire head and the width of the fire front are parameters that can give information about the onset of a wildland fire.

**Funding:** This research received no external funding.

**Institutional Review Board Statement:** Not applicable.

**Informed Consent Statement:** Not applicable.

**Data Availability Statement:** Not applicable.

**Conflicts of Interest:** The authors declare no conflict of interest.

## Appendix A Governing Equations of the Model

The flow behaviour of the gas phase is driven by the following conservation of mass, momentum, and energy equations:

- The conservation of mass equation:

$$\frac{\partial \rho}{\partial t} + \frac{\partial}{\partial x_j}(\rho u_j) = \dot{m}_s^{H_2O} + \dot{m}_s^{pyr} \tag{A1}$$

- The conservation of momentum equation and the turbulence model:

$$\frac{\partial}{\partial t}(\rho u_i) + \frac{\partial}{\partial x_j}\left(\rho u_j u_i - (\mu + \mu_t)\frac{\partial u_i}{\partial x_j}\right) = -\frac{\partial p_d}{\partial x_i} + (\rho - \rho_\infty)g_i + \frac{\partial}{\partial x_j}\left((\mu + \mu_t)\frac{\partial u_j}{\partial x_i}\right) - \frac{2}{3}\frac{\partial}{\partial x_i}\left((\mu + \mu_t)\frac{\partial u_k}{\partial x_k} - \rho k\right) + F_i \tag{A2}$$

Here $F_i$ is the drag force per unit volume acting on the solid-phase particles. It is expressed as follows: $\vec{F} = \frac{1}{8}\alpha_s \sigma_s C_D \rho \left\| \vec{u} \right\| \vec{u}$ where $C_D = \frac{24}{R_e}\left(1 + 0.15 R_e^{0.687}\right)$ is the drag coefficient.

The eddy viscosity $\mu_t$ is given by:

$$\mu_t = C_\mu \rho \frac{k2}{\varepsilon} \tag{A3}$$

$k$ is the turbulent kinetic energy, and $\varepsilon$ is its dissipation rate. The transport equations for $k$ and $\varepsilon$ are deduced from the $k - \varepsilon RNG$ turbulence model [25,26].

$$\frac{\partial \rho k}{\partial t} + \frac{\partial}{\partial x_j}\left[\rho u_j k - \left(\mu + \frac{\mu_t}{\sigma_k}\right)\frac{\partial k}{\partial x_j}\right] = P + W - \rho\varepsilon, \tag{A4}$$

$$\frac{\partial \rho \varepsilon}{\partial t} + \frac{\partial}{\partial x_j}\left[\rho u_j \varepsilon - \left(\mu + \frac{\mu_t}{\sigma_k}\right)\frac{\partial \varepsilon}{\partial x_j}\right] = (C_{\varepsilon 1} P + C_{\varepsilon 3} W - RP)\frac{\varepsilon}{k} - C_{\varepsilon 2}\rho\frac{\varepsilon^2}{k}. \tag{A5}$$

The shear and buoyancy turbulence production/destruction terms $P$ and $W$ can be expressed by

$$P = -\left[\mu_t\left(\frac{\partial u_i}{\partial x_j}+\frac{\partial u_j}{\partial x_i}\right)-\frac{2}{3}\left(\mu_t\frac{\partial u_k}{\partial x_k}+\rho k\right)\delta_{ij}\right]\frac{\partial u_i}{\partial x_j}, \tag{A6}$$

$$W = -\frac{\mu_t}{T\sigma_t}g\frac{\partial T}{\partial x_j}, \tag{A7}$$

with

$$R = \frac{\eta(1-\eta/\eta_0)}{1+\beta\eta^3}, \eta = \sqrt{\left|\frac{P}{\rho C_\mu \varepsilon}\right|} \tag{A8}$$

The constants are given by:

$$\eta_0 = 4.38; \beta = 0.015; C_\mu = 0.0845; C_{\varepsilon 1} = 1.42; C_{\varepsilon 2} = 1.68; C_{\varepsilon 1} = 1.5$$
$$\sigma_k = 0.7179; \sigma_\varepsilon = 1.3; \sigma_t = 0.7$$

- The conservation equation of chemical species and the combustion model

$$\frac{\partial \rho Y_k}{\partial t}+\frac{\partial}{\partial x_j}\left[\rho u_j Y_k-\left(\mu+\frac{\mu}{\sigma_k}\right)\frac{\partial Y_k}{\partial x_j}\right] = \dot{\omega}_k + S_k, \tag{A9}$$

with $k = \{fuel; O_2; CO_2; H_2O; N_2\}$. The source term $S_k$ related to the thermal degradation of the fuel is given by

$$S_k = \begin{cases} (1-\nu_{soot})\alpha_{CO}\dot{m}_s^{pyr} \\ 0 \\ (1-\nu_{soot})(1-\alpha_{CO})\dot{m}_s^{pyr} \\ \dot{m}_s^{H_2O} \\ 0 \end{cases} \tag{A10}$$

The fuel consumption rate is calculated using the Eddy Break Up model [27]. This rate, controlled by the turbulent mixing, is expressed by

$$\dot{\omega}_{CO} = -C_{EBU}\rho\frac{\varepsilon}{k}\min\left(Y_{CO}, \frac{Y_{O_2}}{st}\right) \tag{A11}$$

where $st$ is the stoichiometric ratio of the chemical reaction

$$CO + \frac{1}{2}O_2 \rightarrow CO_2(26) \tag{A12}$$

The rate of consumption or production of other chemical species is related to the fuel consumption $\dot{\omega}_{CO}$,

$$\dot{\omega}_{O_2} = st\dot{\omega}_{CO} \tag{A13}$$

$$\dot{\omega}_{CO_2} = -(1+st)\dot{\omega}_{CO} \tag{A14}$$

- The conservation of energy equation and the radiation model

The energy conservation equation is written for the enthalpy of the gas mixture

$$\frac{\partial \rho h}{\partial t}+\frac{\partial}{\partial x_j}\left[\rho u_j h-\left(\frac{\mu}{Pr}+\frac{\mu_t}{\sigma_h}\right)\frac{\partial h}{\partial x_j}\right] = -Q_{radgaz} - Q_{conv} + S_h \tag{A15}$$

where $h$ is the enthalpy expressed by $h = \sum_\alpha Y_\alpha\left(\Delta h_\alpha + \int_{T_0}^{T} C_{p\alpha}(T)dT\right)$; $\Delta h_\alpha$ is the enthalpy of formation of the species $\alpha$ at the reference temperature $T_0$.

The source term $S_h$ is the energy transfer relative to the mass transfer:

$$S_h = \dot{m}_{H_2O} h_{H_2O} + \dot{m}_{pyr} h_{pyr} \tag{A16}$$

where $h_\alpha$ is the species enthalpy at the temperature of the solid-phase surface.

The divergence of the radiative heat flux can be expressed as

$$Q_{radgaz} = -\frac{\partial q_j^R}{\partial x_j} = \alpha_g a_g \left( G - 4\sigma T^4 \right) \tag{A17}$$

where $G = \int_{4\pi} I\left(\vec{\Omega}\right) d\Omega$ is the irradiance.

The radiation intensity $I\left(\vec{\Omega}\right)$ in the $\vec{\Omega}$ direction is calculated by solving the following radiation transfer equation (RTE)

$$\frac{d}{ds}\left(\alpha_g I^\Omega\right) = \alpha_g a_g \left( \frac{\sigma T^4}{\pi} - I^\Omega \right) + \alpha_s a_s \left( \frac{\sigma {T_s}^4}{\pi} - I^\Omega \right). \tag{A18}$$

The absorption coefficient $a_g$ of the gas mixture is evaluated from the mole fraction of the combustion products $(CO_2, H_2O)$ and the soot volume fraction [27,28]:

$$a_g = 0,1\left(X_{CO_2} + X_{H_2O}\right) + 1862 f_{vs} T. \tag{A19}$$

To calculate the soot volume fraction $f_{vs}$, we assume that some of the fuel is converted to soot [29]. Therefore, the only equation for soot is the following conservation equation for the soot volume fraction,

$$\frac{\partial \rho f_{vs}}{\partial t} + \frac{\partial}{\partial x_j}\left[ \rho \left( u_j + u_j^{th} \right) f_{vs} - \frac{\mu_t}{\sigma_t} \frac{\partial f_{vs}}{\partial x_j} \right] = \dot{\omega}_{fvs} \tag{A20}$$

where $u_j^{th}$ is the mean thermophoretic component in $j$th-direction [30]

$$u_j^{th} = -0.54 \frac{\mu}{\rho} \frac{\partial \ln T}{\partial x_j} \tag{A21}$$

And the term source $\dot{\omega}_{fvs}$ is given by

$$\dot{\omega}_{fvs} = \alpha_6 \frac{\rho}{\rho_{suie}} \dot{m}_s^{pyr} \tag{A22}$$

## References


1. Cruz, M.; Sullivan, A.; Gould, J.; Hurley, R. Got to burn to learn: The effect of fuel load on grassland fire behaviour and its management implications. *Int. J. Wildland Fire* **2018**, *27*, 727–741. [CrossRef]
2. Cheney, N.; Gould, J. Fire growth in grassland fuels. *Int. J. Wildland Fire* **1995**, *15*, 237–247. [CrossRef]
3. Cheney, N.; Gould, J.; Catchpole, W. Prediction of fire spread in grasslands. *Int. J. Wildland Fire* **1998**, *8*, 1–13. [CrossRef]
4. Sutherland, D.; Sharples, J.; Moinuddin, K. The effest of ignition protocol on grassfire developpment. *Int. J. Wildland Fire* **2019**, *129*, 70–80.
5. Atchley, A.; Linn, R.; Jonko, A.; Hoffman, C.; Hyman, J.; Pimont, F.; Sieg, C.; Middleton, R. Effect of fuel spatial distribution on wildland fire behaviour. *Int. J. Wildland Fire* **2021**, *30*, 179–189. [CrossRef]
6. Vanella, M.; McGrattan, K.; McDermott, R.; Forney, G.; Mell, W.; Gissi, E.; Fiorucci, P. A Multi-Fidelity Framework for Wildland Fire Behavior Simulations over Complex Terrain. *Atmosphere* **2021**, *12*, 273. [CrossRef]
7. Porterie, B.; Morvan, D.; Loraud, J.; Larini, M. Firespread through fuel beds: Modeling of wind—Aided fires and induced hydrodynamics. *Phys. Fluids* **2000**, *17*, 1762–1782. [CrossRef]
8. Porterie, B.; Consalvi, J.; Loraud, J.; Giroud, F.; Picard, C. Dynamics of wildland fires and their impact on structures. *Combust Flame* **2007**, *149*, 314–328. [CrossRef]

9. Brou, A.; Adou, K. Modelling the Effect of Grassland Fuel Bed Structure on the Headfire Rate of Spread. *Combustion Sci. Technol.* **2022**. [CrossRef]
10. Gronli, M. A theoretical and Experimental Study of Thermal Degradation of Biomaa. Ph.D. Thesis, The Norwegian University of Science and Technology, Faculty of Mechanical Engineering, Department of Thermal Energy and Hyfropower, Trondheim, Norway, 1996; p. 342.
11. Alen, R.; Kuoppala, E.; Oesch, P. Formation of the main degradation compound groups from wood and its components during pyrolysis. *J. Anal. Appl. Pyrolysis* **1996**, *36*, 137–148. [CrossRef]
12. Di Blasi, C. Comparison of semi-global mechanisms for primary pyrolysis of lignocellulosic fuels. *J. Ana. Appl. Pyrolysis* **1998**, *47*, 43–64. [CrossRef]
13. Di Blasi, C.; Branca, C.; Santoro, A.; Gonzalez, H. Pyrolytic behavior and products of some wood varieties. *Combust. Flame* **2001**, *47*, 165–177. [CrossRef]
14. Branca, C.; Albano, A.; Di Blasi, C. Critical evaluation of global mechanisms of wood devolatilization. *Thermochim. Acta.* **2005**, *429*, 133–141. [CrossRef]
15. Yang, H.; Yan, R.; Chen, H.; Lee, D.; Zheng, C. Characteristics of hemicellulose, cellulose and lignin pyrolysis. *Fuel* **2007**, *86*, 1781–1788. [CrossRef]
16. Pagni, P.; Peterson, T. Flame spread through porous fuel. *Symp. (Int.) Combust.* **1973**, *14*, 1099–1107. [CrossRef]
17. Morvan, D.; Dupuy, J. Modeling the propagation of a wildfire through a Mediteranean shrub using a multiphase formulation. *Combust. Flame* **2004**, *138*, 199–210. [CrossRef]
18. Incropera, F.; Dewitt, D. *Fundamentals of Heat and Mass Transfert*, 4th ed.; John Wiley & Son: Hoboken, NJ, USA, 1985.
19. De Mestre, N.J.; Catchpole, E.A.; Anderson, D.H. Uniform propagation of a planar fire front without wind. *Combust. Sci. Technol.* **1989**, *65*, 231. [CrossRef]
20. Koo, E.; Pagni, P.; Woycheese, J.; Stephens, S.; Weise, D.; Huff, J. A simple physical model for forest fire spread rate. *Proc. Fire Saf. Sci.* **2005**, *8*, 851–862. [CrossRef]
21. Bard, S.; Pagni, P. Spatial Variation of Soot Volume Fractions in Pool Fire Diffusion Flame. In *Fire Safety Science, Proceeding of the First International Symposium, International Association for Fire Safety Science, Gaithersburg, MD, USA, 7–11 October 1985*; Springer: London, UK, 1985; pp. 361–369.
22. Susott, R. Characterization of the thermal properties of forest fuel by combustible gas analysis. *For. Sci.* **1982**, *2*, 404–420.
23. Dupuy, J.; Morvan, D. Numerical study of a crown fire spreading toward a fuel break using a multiphase physical model. *Int. J. Wildland Fire* **2005**, *14*, 141–151. [CrossRef]
24. Moinuddin, K.; Sutherland, D.; Mell, W. Simulation study of grass fire using a physics—Based model: Striving towards numerical rigour and the effect of grass height on the rate of spread. *Int. J. Wildland Fire* **2018**, *27*, 800–814. [CrossRef]
25. Yakhot, V.; Orszag, S.A. Renormalization group analysis of turbulence. *J. Sci. Comput.* **1986**, *1*, 3–51. [CrossRef]
26. Yakhot, V.; Smith, L.M. The renormalization group, the e-expansion and derivation of turbulence models. *J. Sci. Compt.* **1992**, *7*, 35–61. [CrossRef]
27. Magnussen, B.F.; Hjertager, B.H. On mathematical modelling of turbulent combustion with special emphasis on soot formation and combustion. *Symp. (Int.) Combust.* **1977**, *16*, 719–729. [CrossRef]
28. Kent, D.R.; Honnery, J.H. A soot formation rate map for a laminar ethylene diffusion flame. *Combust. Flame* **1990**, *79*, 287–298. [CrossRef]
29. Novozhilov, V.; Moghtaderi, B.; Fletcher, D.F.; Kent, J.H. Computational fluid dynamics modelling of wood combustion. *Fire Saf. J.* **1996**, *27*, 69–84. [CrossRef]
30. Kaplan, C.R.; Shaddix, C.R.; Smyth, K.C. Computations of enhanced soot production in time-varying CH4/Air diffusion flame. *Combust. Flame* **1996**, *106*, 392–404. [CrossRef]